Tunable Resonator-Upconverted Emission (TRUE) Color Printing and Applications in Optical Security

Hailong Liu, Jiahui Xu, Hao Wang, Yejing Liu, Qifeng Ruan, Yiming Wu, Xiaogang Liu,* and Joel K. W. Yang*

Lanthanide-doped nanophosphors are promising in anti-counterfeiting and security printing applications. These nanophosphors can be incorporated as transparent inks that fluoresce by upconverting near-infrared illumination into visible light to allow easy verification of documents. However, these inks typically exhibit a single luminescent color, low emission efficiency, and low print resolutions. Tunable resonator-upconverted emission (TRUE) is achieved by placing upconversion nanoparticles (UCNPs) within plasmonic nanoresonators. A range of TRUE colors are obtained from a single-UCNP species self-assembled within size-tuned gap-plasmon resonances in Al nanodisk arrays. The luminescence intensities are enhanced by two orders of magnitude through emission and absorption enhancements. The enhanced emissive and plasmonic colors are simultaneously employed to generate TRUE color prints that exhibit one appearance under ambient white light, and a multicolored luminescence appearance that is revealed under near-infrared excitation. The printed color and luminescent images are of ultrahigh resolutions (≈50 000 dpi), and enable multiple colors from a single excitation source for increased level of security.

Lanthanide-doped upconversion nanoparticles (UCNPs) are nonlinear optical materials that luminesce through an upconversion process by absorbing lower-energy photons in the near-infrared region and emitting high-energy photons in the visible or ultraviolet.[1–3] Unlike other nonlinear optical properties, such as second/third-harmonic generation[4,5] and two-photon

Dr. H. Liu, Dr. H. Wang, Dr. Y. Liu, Dr. Q. Ruan, Prof. J. K. W. Yang
Singapore University of Technology and Design
8 Somapah Road, Singapore 487372, Singapore
E-mail: joel_yang@sutd.edu.sg
J. Xu, Y. Wu, Prof. X. Liu
Department of Chemistry
National University of Singapore
Singapore 117543, Singapore
E-mail: chmlx@nus.edu.sg
Dr. Q. Ruan
SZU-NUS Collaborative Innovation
Center for Optoelectronic Science & Technology
International Collaborative Laboratory of 2D Materials for
Optoelectronics Science and Technology of Ministry of Education
College of Optoelectronic Engineering
Shenzhen University
Shenzhen 518060, China
Prof. J. K. W. Yang
Institute of Materials Research and Engineering (IMRE)
2 Fusionopolis Way, Innovis, #08-03, Singapore 138634, Singapore

photoluminescence,[6] UCNPs can be excited using continuous wave (CW) lasers, instead of pulsed lasers with high peak powers. In addition, UCNPs exhibit large anti-Stokes shifts, narrow emission bands, chemical stability, and high photostability.[7–9] These properties make them promising for applications in biomedical sensors,[10,11] volumetric displays,[12–14] solar cells,[15,16] infrared detectors,[17] and optical document security.[18–24] While optical security based on UCNPs has been demonstrated, there are limitations to the current approach of incorporating UCNPs as inks to print hidden images onto paper or plastic substrates.[20–24] Efforts are needed to overcome limitations in emission efficiency, print resolution, and the range of luminescent colors to enable new functionalities of UCNPs in security printing.

Current methods to achieve a range of upconverted luminescent colors include doping with different lanthanide elements,[25,26] tuning lanthanide concentrations,[27] varying temperatures,[28] controlling the grain sizes,[29] and changing excitation wavelengths or laser powers.[30,31] However, these methods require sequential deposition and placement of multiple UCNP types, and/or complex illumination sources to achieve multiple luminescent colors. For instance, UCNPs of different types need to be precisely positioned next to each other to achieve two juxtaposed luminescent colors. Furthermore, complex illumination methods can create colorful luminescent images but in this case the substrate containing UCNP acts as a blank screen while information is imparted by the illumination to form arbitrary images.[12] To simplify the fabrication and imaging of security prints, it is thus desirable to develop a platform to obtain multiple luminescent colors using one type of UCNP under a single CW excitation source. The integration of UCNPs with plasmonic nanostructures reported here enables this simplification while enhancing emission efficiency and print resolution.

Plasmonic nanostructures have the ability to greatly enhance near-field electromagnetic fields through coupling light in/out of ultrasmall volumes beyond the optical diffraction limit.[32–34] This effect is used to enhance the luminescence of quantum emitters, e.g., quantum dots,[35] 2D materials,[36] fluorescent molecules,[37] and upconversion nanocrystals.[38–50] Although some plasmonic nanostructures have been employed to enhance upconversion luminescence, their resonances are

**ADVANCED
SCIENCE NEWS**

www.advancedsciencenews.com

**ADVANCED
MATERIALS**

www.advmat.de

merely spectrally aligned with either the absorption or one emission band of UCNPs.[39–43] Systematic studies are currently lacking on tuning the upconversion colors and enhancing the luminescence intensities with plasmonic nanostructures through both absorption and emission enhancements.

Plasmonic color generation[51] realized through metallic nanostructures is a promising approach for next generation color prints, display devices, and optical security elements with unrivaled print resolution, high-throughput manufacturing, and durability.[52–54] In addition to the effects such as size-dependent colors and the inherent ultrahigh resolution achievable by plasmonic color prints, one can increase the level of security of these prints by incorporating fluorescent materials. Judicious integration of plasmonic color prints with UCNPs could provide enhanced luminescence to UCNPs, new functionality to plasmonic colors, and increased level of secrecy of the combined prints. Prints could exhibit one set of information under white light, with covert information under near-infrared light to deter counterfeiting. However, incorporating UCNPs into lithographically-defined pixels and realizing covert luminescent information remains a nanofabrication challenge.

Here, we overcome the challenges in nanofabrication to realize tunable resonator-upconverted emission (TRUE) color printing, which displays an ultrahigh resolution color print under ambient white light, while an upconversion luminescence image is only revealed upon excitation with a near-infrared CW laser. Our process minimizes the use of lanthanide-doped UCNPs to a monolayer thick coverage sandwiched between aluminum nanodisks and a back-reflector. Doing so, places the UCNPs in the hotspot of a gap plasmon mode, thus allowing Purcell factor enhancement of luminescence. The luminescence intensities are enhanced by two orders of magnitude when plasmonic resonances are aligned with the

emission bands of UCNPs. Importantly, the relative intensities of these emission bands can be manipulated to realize a range of luminescent colors. We introduce an empirical equation that allows the contribution of enhanced absorption and emission to be quantified. We observe that both enhanced excitation and radiative decay rates underpin the enhanced upconversion luminescence. Finally, we demonstrate the covert incorporation of different upconversion luminescence images under a plasmonic color print, with potential application in optical documental security.

Figure 1a shows the schematic of our TRUE color pixels, in which each pixel consists of a 2×2 array of metal-UCNPs-metal (MUM) nanostructures, i.e., Al-disk/SiO$_2$/UCNPs/Al-film. The pixels display specific visible colors under white light due to the collective resonant oscillation of free electrons in the metals constituting the MUM nanostructures. The colors of these pixels are determined by the local environment and geometric parameters, e.g., diameter of disks (D), separations (s) between disks, and distances (t) between Al disks and the bottom Al film. As such, we are able to print high-resolution color images by lithographically defining different sized disks on a substrate to achieve the corresponding colors.

In addition to the reflected colors observed under ambient bright-field illumination, the UCNPs sandwiched in the ultrasmall gaps will luminesce in the visible spectrum when excited by a near-infrared laser. Figure 1b shows the scanning electron microscope (SEM) image of assembling UCNPs in lithographically patterned poly(methyl methacrylate) (PMMA) holes, and Figure 1c gives the corresponding TRUE color pixels with UCNPs sealed in the ultrasmall gaps. The UCNPs are placed in the region of enhanced electromagnetic fields of the gap-plasmon mode.[55] Thus, the emitters experience a large Purcell factor enhancement through plasmon-emitter coupling.[56,57] By
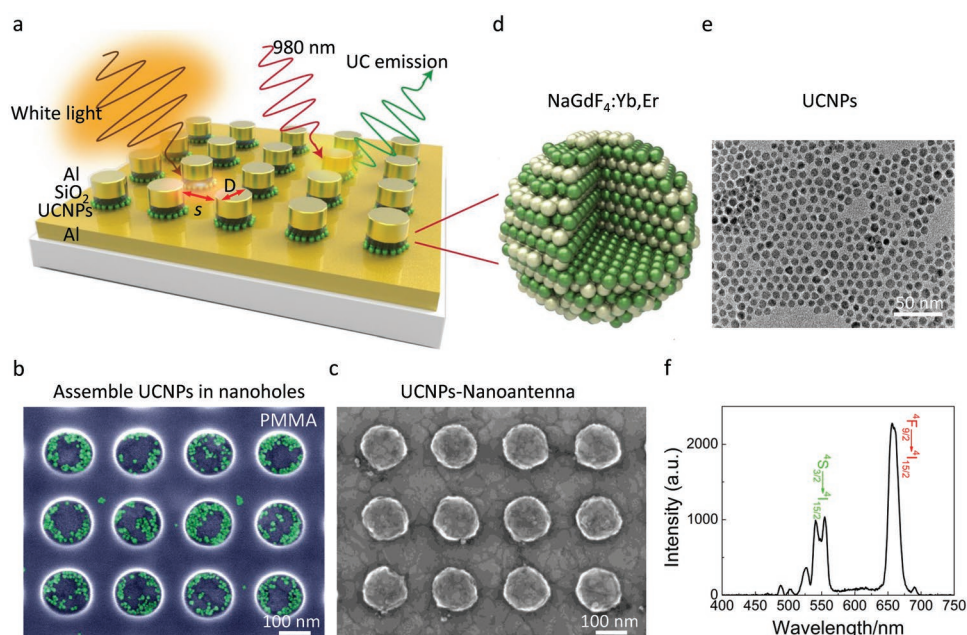

Figure 1. TRUE color pixels. a) Schematic showing TRUE color pixel arrays. Each pixel consists of a 2×2 array of disks arranged in a square array of constant pitch. b) SEM image of the assembled UCNPs in PMMA nanoholes with $D = 130$ nm and $s = 100$ nm. c) SEM image of the fabricated pixel arrays with $D = 130$ nm and $s = 100$ nm. d–f) 3D layout, TEM, and luminescence spectrum of 10 nm NaGdF$_4$:Yb,Er nanocrystals.

tuning the plasmonic resonances of MUM nanostructures and matching them with the energy level transitions of lanthanide ions, we can selectively manipulate different emission channels of UCNPs to get different luminescent colors. Hence, the intensities and colors of luminescence in each pixel are also determined by the plasmonic resonances of TRUE color pixels, and an enhanced luminescence image can be observed in the same area of the patterned plasmonic color prints with illuminating near-infrared laser light.

The enhancement factor of emission for an emitter placed in a cavity is given by the Purcell factor, $P = (3/4\pi^2)(\lambda/n)^3(Q/V)$, where λ and n are the incident wavelength and the average refractive index, V and Q refer to the mode volume and quality factor of the cavity.[57] It has been shown that the combination of ultrathin MUM geometries with the lateral confinement of resonator structures can yield cavities with ultrasmall mode volumes.[55,56] As the size of UCNPs define the gap of the MUM resonator, to achieve a small mode volume and high Purcell factor enhancement, we synthesized NaGdF$_4$:Yb,Er nanocrystals of ≈10–20 nm diameters, as shown in the transmission electron micrograph (TEM) in Figure 1e. Figure 1d shows the 3D

schematic representation of a single NaGdF$_4$:Yb,Er nanocrystal, in which NaGdF$_4$ is the local host and Yb^{3+} ions are the sensitizers that absorb 980 nm wavelength photons and excite the activators (Er^{3+} ions) through energy transfer.[1–3] The excited Er^{3+} ions are promoted to a higher energy state after absorbing a second photon or undergoing an energy transfer process, resulting in radiative decay through several available transitions between different energy levels.[1–3] The luminescence spectrum of NaGdF$_4$:Yb,Er nanocrystals is shown in Figure 1f. Two main emission peaks at 545 (the green emission band) and 655 nm (the red emission band) are observed in the visible region. These two peaks correspond to the transitions of Er^{3+}, from $^4S_{3/2}$ to $^4I_{15/2}$ and from $^4F_{9/2}$ to $^4I_{15/2}$, respectively.[45–47] The energy level diagram of NaGdF$_4$:Yb,Er nanocrystals is presented in Figure S1 (see Supporting Information).

To investigate the coupling effects between our plasmonic MUM nanostructures and UCNPs, we fabricated a series of TRUE color pixels with varying diameter D and separation (s), as shown in **Figure 2**. The fabrication steps and details are described in Figure S2 (see Supporting Information) and in the Experimental Section. Figure 2a shows the SEM images i),
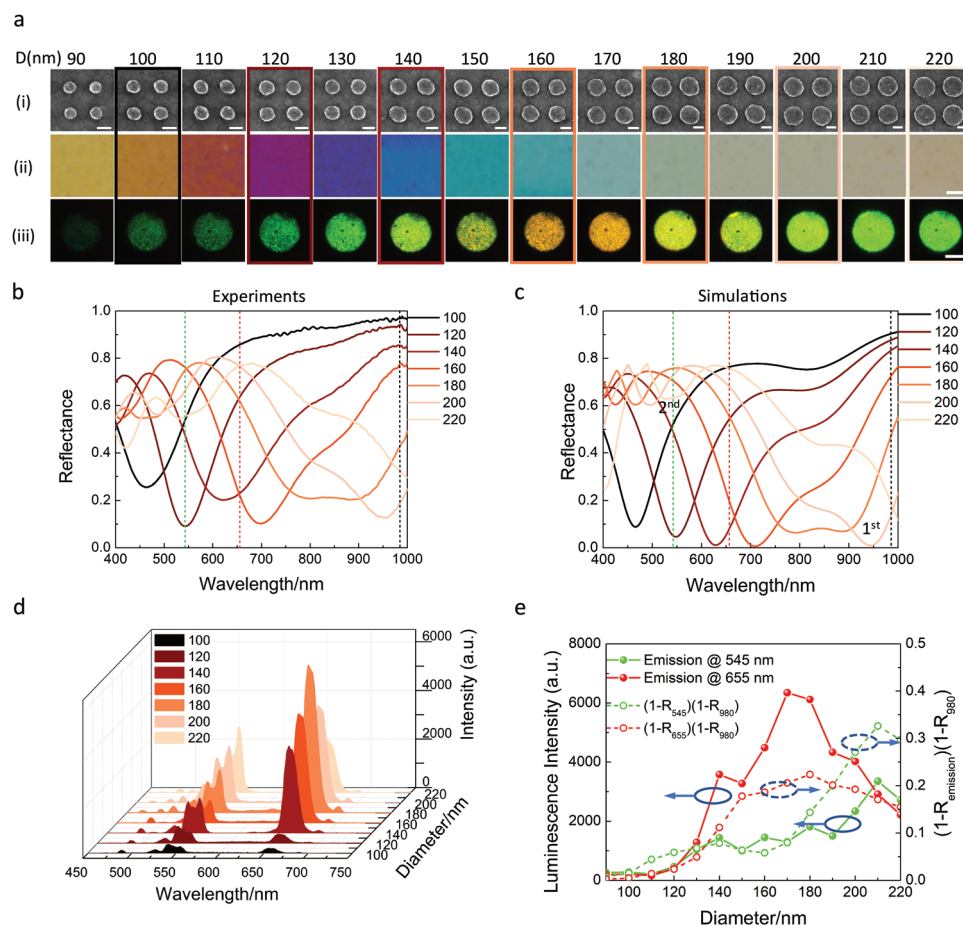

Figure 2. Optical properties of TRUE color pixels. a) SEM i), reflected bright field ii), and upconversion luminescence iii) color patches of pixel arrays with D = 90–220 nm and s = 100 nm. b,c) Measured and simulated reflectance spectra of TRUE color pixels in (a). d) Upconversion luminescence of pixel arrays with D = 100–220 nm. e) The product of $(1 - R_{emission})(1 - R_{980})$ (right y-axis) and the upconversion luminescence intensity of green and red emission bands (left y-axis) as a function of Al disk diameter. R_{545}, R_{655}, and R_{980} represent the reflectivity of the TRUE color pixels at 545, 655, and 980 nm, respectively. $1 - R_{545}$, $1 - R_{655}$, and $1 - R_{980}$ are employed to get estimation of the absorbance of UCNPs at these three wavelengths. Scale bars: i) 100 nm; ii,iii): 10 µm.

**ADVANCED
SCIENCE NEWS**

www.advancedsciencenews.com

**ADVANCED
MATERIALS**

www.advmat.de

color patches ii), and the corresponding luminescent images iii) of the fabricated TRUE color pixels with $D = 90$–220 nm and $s = 100$ nm. Color palettes with $s = 70$ and 150 nm are given in Figure S3 (see Supporting Information). From these color palettes, we observe a range of plasmonic colors including yellow, orange, purple, blue, and green. The measured reflectance spectra are in good agreement with the simulated ones, as shown in Figure 2b,c, respectively. The plasmonic resonances of our pixels range from 400 to 1000 nm, i.e., spanning the range of emission and excitation wavelengths of the UCNPs. Such a large range of resonances allows us to gradually tune the spectral overlap between TRUE color pixels and UCNPs to explore different enhancement effects, i.e., plasmonic resonances coupling with the emission bands (the green and red dash lines in Figure 2b) or the absorption band (the black dash line in Figure 2b) of NaGdF$_4$:Yb,Er.

The variations in luminescent micrographs (Figure 2a-iii) show that colors can be tuned from green→yellow→orange→ yellow→green as the nanodisk diameter was varied from 90 to 220 nm for a constant separation (s) of 100 nm. More than two luminescent colors were achieved by tuning the plasmonic resonances from 400 to 1000 nm, to enable colorful luminescence images. To quantify the emission intensities, we measured the upconversion luminescence spectra under 980 nm excitation (details in the Experimental Section). Figure 2d presents the measured results showing variation in luminescence intensities and ratios between the red and green bands as a function of disk diameter. The intensities of each band are plotted in Figure 2e. The green band shows an overall monotonic increase with diameter despite some fluctuations. Conversely, the red emission band exhibits a clear peak in intensity at $D = 170$ nm. The varying ratios of green to red bands lead to different luminescence colors even with the simple disk geometry. For instance, the larger Purcell enhancement for red compared to the green band at $D = 170$ nm explains the orange luminescent color in Figure 2a-iii. Conversely, a bright green luminescence is observed at $D = 210$ nm where the first order gap plasmon mode is spectrally matched to the absorption while the second order mode enhances the green emission. The results demonstrate that the emission bands can be selectively manipulated or enhanced by tuning the resonances of the plasmonic structures embedding UCNPs.

To quantify the enhancement in luminescence, we compared the relative intensity of the upconversion luminescence from the TRUE color pixels with that of a reference sample, prepared in the same way as the TRUE color samples except that the Al deposition step was skipped. It thus consists of UCNPs self-assembled into disks on an aluminum substrate minus the Al disks. Figure S4 (Supporting Information) compares the two cases at maximum emissions at $D = 210$ nm for the green peak and $D = 170$ nm for the red one. The maximum enhancements were measured to be 90 and 180 times for the green and red emission bands, respectively.

Plasmon enhanced luminescence are attributed to the enhancement in both the absorption of the excitation laser and Purcell-factor enhancement of the emission. The enhancement depends on the spectral alignment between plasmonic resonances and the absorption or emission frequencies.[43–47,49,50] Here, we introduce a simple empirical equation to quantify the

degree of spectral matching between the absorption and emission wavelengths. The absorbance of the UCNPs at 980 nm excitation laser is estimated to be $1 - R_{980}$, where R_{980} is the measured reflectance of TRUE color pixels at 980 nm (the black dashed line in Figure 2b). It is noted that enhanced emission also occurs within the broad plasmon resonances due to the large local density of optical states that increase radiative decay rates.[44] We employ $1 - R_{545}$ and $1 - R_{655}$ as a measure of the spectral matching of TRUE color pixels with UCNPs emissions at 545 and 655 nm, where R_{545} and R_{655} are the measured reflectivity of TRUE color pixels (the red and green dash lines in Figure 2b), respectively. Thus, we use the product of the absorbances at 980 nm and at the spectral matching at emission frequencies, i.e., $(1 - R_{545})(1 - R_{980})$ and $(1 - R_{655})$ $(1 - R_{980})$, to qualitatively predict the enhancement of the upconverted luminescence, as shown in Figure 2e. Remarkably, this simple equation can accurately track the trends of the luminescence intensity of both the green and red bands. Therefore, plasmonic enhanced upconversion luminescence can be qualitatively predicted by tracking the relative spectral alignment of plasmon resonances and UCNP transitions, which provides insight for designing TRUE color pixels.

To investigate the plasmonic enhanced absorption and emission processes of NaGdF$_4$:Yb,Er in TRUE color pixels, we modeled the pixel arrays using a finite-difference time-domain software (Lumerical FDTD Solutions, see the Experimental Section) and calculated the absorption spectra, the corresponding near-field electromagnetic field enhancement at the absorption wavelength, and the spontaneous emission enhancement in emission bands, i.e., radiative decay rate and Purcell factor.[44,55–59]

For plasmon enhanced absorption, the absorption at 980 nm and the electric-field intensity ($|E|^2$) at 980 nm are the most important parameters that determines the excitation rate of the sensitizer (Yb^{3+}), which transfers energy to Er^{3+} to emit photons after a second photon absorption and energy transfer process. The calculated absorbance at 980 nm as a function of the diameter (D) of disks is given in Figure S5 (Supporting Information). The simulated absorbance reaches its maximum at $D = 210$ nm, in agreement with structures with $D = 210$ nm and $s = 100$ nm having the largest excitation rates. Moreover, we select this size of MUM to investigate the position-dependent (electric-field-intensity-dependent) excitation of Yb^{3+} within one nanostructure. **Figure 3**a–c shows the electric-field distributions ($|E|$ in xy and xz plane) at different positions inside the nanodisk with the incidence light of 980 nm. The maximum intensity of the electric-field is in the MUM gap (the dielectric cavity separating the disk from the metal layer) that provides the largest excitation rate and luminescence intensity than other positions in this nanostructure, as verified in control experiments. We selected the MUM gap and the top surface of disks as two different positions, marked with 1 and 2 in Figure 3a to assemble UCNPs and compared the enhancement. Position 1 has larger electric-field intensity ($|E|$ in xy plane) than position 2, as shown in Figure 3b,c. Figure S6 (Supporting Information) compares the enhanced luminescence with assembly of UCNPs at positions 1 and 2. It is noted that the sample with UCNPs at position 1 has an eightfold enhancement compared to the sample with UCNPs at position 2 for the red emission
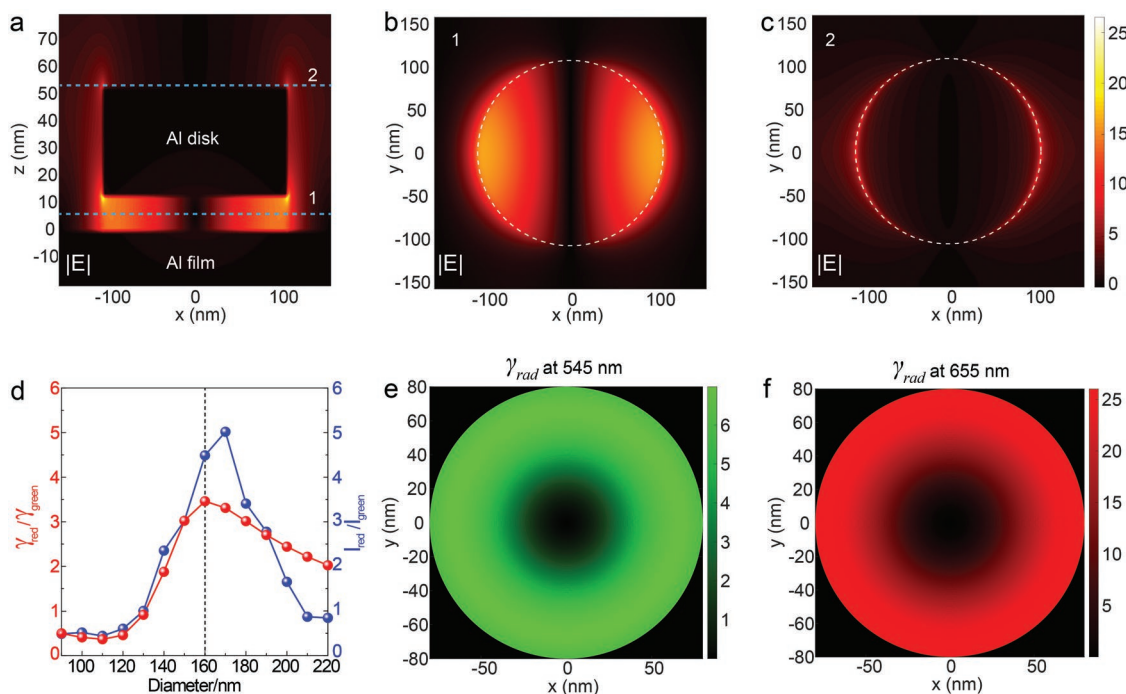
**ADVANCED
SCIENCE NEWS**
www.advancedsciencenews.com

**ADVANCED
MATERIALS**
www.advmat.de

Figure 3. Enhanced absorption and radiative decay. a) Cross-sectional electric-field distributions ($|E|$ in xz plane) of MUM with $s = 100$ nm and $D = 210$ nm. b,c) Near-field electric-field distributions ($|E|$ in xy plane) at the center of the MUM gap (position 1) and on the surface of the devices (position 2) in (a). The resonant wavelength is 980 nm. The color bar is applicable to the Figure (a–c). d) The ratio of radiative decay rate between green and red channel (545 and 655 nm) as a function of the diameter (D) of disks (red line). Measured integration ratio of red to green emission band intensity (I_{red}/I_{green}, the blue line). I_{red} and I_{green} for each diameter are calculated from the experimental results in Figure 2d with integrating the intensity at wavelength band 630–680 and 525–575 nm for red and green channel, respectively. e,f) Radiative decay rate mapping of the MUM with $D = 160$ nm and $s = 100$ nm at the center of the cavity under 545 and 655 nm, respectively. For each pair of coordination (x and y), the radiative decay rate is an average value by inserting a dipole in three orthogonal directions.

peak. Hence, positions with higher electric-field intensity at 980 nm have higher excitation rates.

To determine the plasmon enhanced emission, we aligned a dipole in the MUM gap oriented along the x, y, and z directions and calculated the averaged radiative decay rate (radiative decay rate γ_{rad} is defined as the enhanced radiative emission of the plasmonic structure with dipole inside the cavity with respect to the dipole-self without plasmonic nanostructures.) and Purcell factor for both red and green emission bands, as shown in Figures S7 and S8 (see Supporting Information). Figure S7c (Supporting Information) gives the calculated Purcell factors for green and red emission bands, which are in good agreement with the luminescence intensity trends in Figure 2e. Therefore, Purcell factor enhancement is the other important factor for plasmonic enhanced luminescence in TRUE color pixels. To accurately show how plasmonic enhanced radiative decay of UCNPs, Figure S7d (Supporting Information) shows the function of the calculated radiative decay rate with respect to the disk diameter (D). The resulting trend is similar to the measured luminescence intensity as a function of disk diameter for the red emission channel (Figure 2e). Thus, plasmonic enhanced radiative decay rate in red emission area is plausibly the dominant factor of luminescence enhancement. On the other hand, the simulated radiative decay rate for green emission channel (Figure S7d, Supporting Information) does not match the trend of the luminescence intensity for the green emission channel (Figure 2e). This disagreement is consistent

with the dominant influence of enhanced absorption on green luminescence.

To separate the influence of radiative decay rate from that of absorption at 980 nm, we calculated the ratio of the radiative decay rate of the red (655 nm) to the green (545 nm) bands for $D = 90$–220 nm, and compared them to the ratio of the integrated measured intensity of red to green bands, as shown in Figure 3c. As the absorption enhancement is the same for both emission bands at a given disk diameter, dividing the emission intensities enables us to determine their relative emission enhancements. The red line is the ratio of the radiative decay rates ($\gamma_{red}/\gamma_{green}$), where γ_{red} and γ_{green} are the averaged radiative decay rates of red and green bands, respectively. The ratio of the integrated intensity of red to green emission bands (I_{red}/I_{green}, the blue line in Figure 3d) are obtained from the experimental results in Figure 2d. Overall, these two ratios are in good agreement with each other with D smaller than 200 nm, and hence the enhanced radiative decay rates can explain the plasmonic enhanced luminescence with $D = 90$–200 nm.

We also investigate the position-dependent radiative decay rate in the MUM cavity between Al disk and the bottom Al film. Figure 3e,f shows the map of radiative decay rates at 545 and 655 nm within the cavity of the MUM with $D = 160$ nm and $s = 100$ nm. For $D = 160$ nm, the maximum of the plasmonic enhanced radiative decay rate for each of these two emission peaks is at the edges of disks and the minimum values are in the center. This result shows that UCNPs trapped around the

edges are responsible for most of the luminescence enhancement, with minimal emission from particles in the center. Our UCNPs are actually assembled around the edges of disks, as shown in Figure 1b. It should be noted that the radiative decay rate of MUM with $D = 160$ nm at 655 nm is around three to four times larger that of the green peak (545 nm). This result corroborates with the experimental observation of the four times stronger luminescence in the red than in the green for disks with $D = 160$ nm in Figure 3d.

In the following, we demonstrate a security feature based on TRUE color printing. First, we select the layout for security prints and measure the nominal (R, G, and B) values for each pixel, and then calculate the color difference (Euclidean distance) between the nominal pixel color and the measured color patches in Figure 2 and Figure S3 (Supporting Information), selecting the color patch with minimum distance as the pixel color to be achieved with fabrication and correspondingly determining the parameters (D and s) for the disks. We printed the designed security prints by following the fabrication process flow in Figure S2 (Supporting Information).

As a first demonstration, we printed color images that exhibit a different luminescent color scheme of the same image, as presented in **Figure 4**. Figure 4a is a bright-field optical micrograph of a plasmonic butterfly, observed under white light illumination. The disks are patterned on a fixed grid of 520 nm pitch, resulting in a resolution of $\approx 5 \times 10^4$ dpi. We employed a $\times 100$ lens with NA of 0.9 to observe details of the high-resolution luminescence images (Figure 4b). Figure 4b-i,ii presents the enhanced upconversion luminescence images of the right wing i) and the tail ii) of the printed butterfly. Figure S9 (see Supporting Information) shows the effects of excitation

laser power on the butterfly luminescence image. Note that the excitation laser power affects the brightness and has negligible effect on the hue of the emission. For UCNPs, in addition to the excitation laser power, the emission efficiency decreases with decreasing size due to surface quenching effects.[44] To increase the brightness of the upconversion luminescence image for ease of authentication, we employed larger diameter, i.e., 20 nm, NaYF$_4$:Yb,Er (Figure S10, Supporting Information) in MUM nanostructures and patterned the art of "The Starry Night" (Vincent van Gogh, 1889). The plasmonic color printing and the corresponding luminescence image are shown in Figure 4c,d, respectively. We can clearly see the details of the prints in both two cases.

The upconversion luminescence images show different colors upon 980 nm laser excitation as compared with plasmonic color prints observed under white light source (Figure 4). Here, the color serves as one dimension of encryption even with the same layout and blueprint. Next, we increase the complexity of our platform by adding more dimensions of encryption in which the upconversion color prints are different from and hidden under the plasmonic color prints (**Figure 5**).

Figure 5 shows results of encoding luminescent letters "UCNP" and a luminescent football into a nonluminescent butterfly. It was achieved with two-step electron beam lithography (EBL) method. In the first step of EBL, the nonluminescent butterfly excluding the letters "UCNP" and the football, as shown in Figure S11 (Supporting Information), was achieved with the fabrication steps in Figure S2 (Supporting Information). To make the butterfly nonluminescent, we used the NaGdF$_4$ nanocrystals instead of NaGdF$_4$:Yb,Er as the sandwiched nanoparticles. Due to the absence of rare-earth ions of Yb^{3+} and Er^{3+}, NaGdF$_4$ nanocrystals would not emit luminescence under 980 nm laser illumination. In the second step of EBL, we patterned the letters "UCNP" and the football into the corresponding blank areas of the butterfly sample achieved in the first step of EBL. The luminescent NaGdF$_4$:Yb,Er nanoparticles were used as the sandwiched nanoparticles. To accurately align the two steps of EBL, three markers were used to reduce the alignment error. The misalignment between these two steps was less than 100 nm, as shown in the SEM images (Figure 5c). It should be mentioned that the sizes, shapes, concentrations, and spin-coating parameters for NaGdF$_4$ and NaGdF$_4$:Yb,Er nanocrystals in these two steps should be the same to keep the colors of "UCNP" and football continuous with the remaining parts to hide them into the background when viewed under white light. Figure 5a shows the bright-field optical micrograph of the plasmonic butterfly after inserting the luminescent "UCNP" and football into the corresponding blank areas. The letters "UCNP" are nearly perfectly matched with the surrounding as seen in the magnified optical micrograph, exhibiting little if any color difference. It is worth mentioning that the lanthanide-doped materials of Yb^{3+} and Er^{3+} rarely affect the plasmonic behavior in the pixels so that the two components are not differentiated under the white-light bright-field microscope (Figure 5a). Due to the dose nonuniformity of write-field with 30 kV (E-line plus Raith), the colors of football have bigger color difference with surrounding pixels than that for "UCNP," and this color difference can be solved with fine adjusting the writing dose factors for different areas.
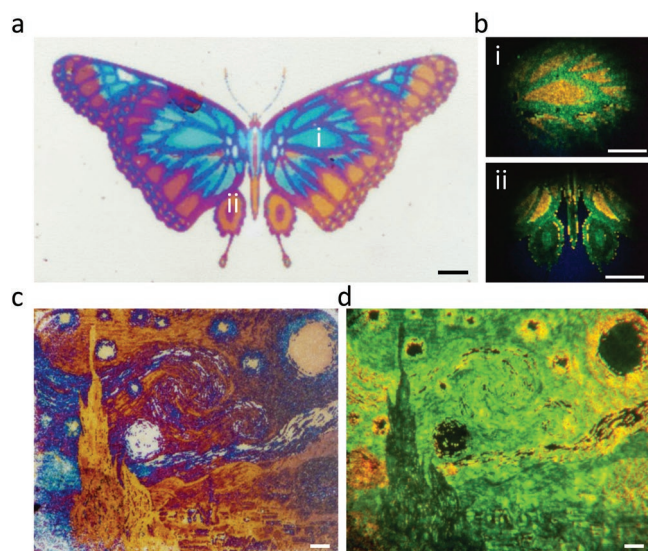

Figure 4. TRUE color prints. a,b) Bright-field optical micrograph of a plasmonic butterfly and its corresponding luminescence images. Luminescence images i,ii) taken with 100 × lens (NA = 0.9), show the enhanced upconversion luminescence information of the right wing and the tail area of the butterfly. 10 nm NaGdF$_4$:Yb,Er nanocrystals are employed as UCNPs in this print. c,d) Optical micrograph and its corresponding luminescence image (taken with 50 × lens, NA = 0.8) of "The Starry Night" (Vincent van Gogh, 1889) using 20 nm NaYF$_4$:Yb,Er as UCNPs. Scale bars: 10 µm.
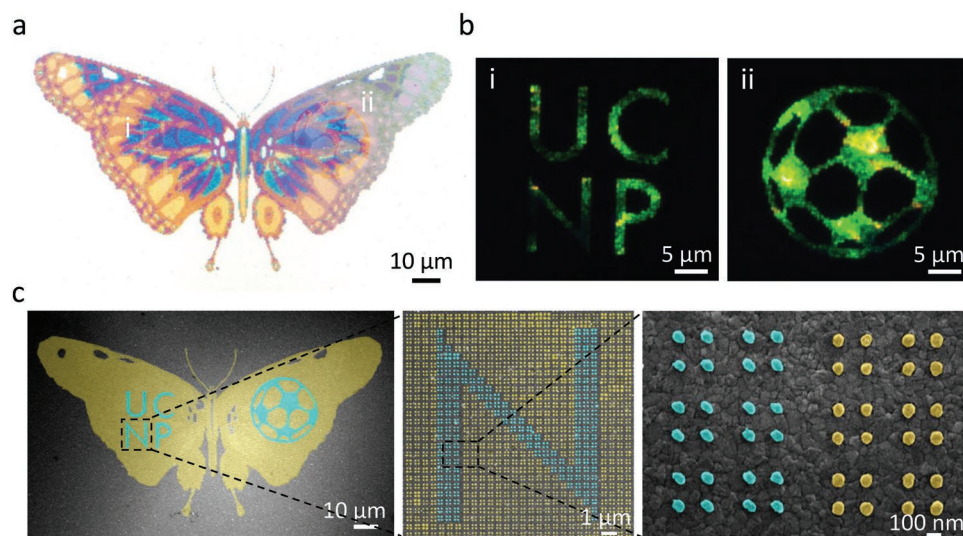
Figure 5. Embedded covert upconversion luminescence images within plasmonic color prints. a) Optical micrograph of a nonluminescent butterfly with covert letters "UCNP" and a football. b) Luminescent images of the hidden letters "UCNP" i) and football ii) revealed under near-infrared excitation. c) Pseudo color SEM images of the plasmonic butterfly with "UCNP" and football. Magnified SEM images of the area of "N" showing a small misalignment of ≈100 nm between the electron-beam lithography steps.

Figure 5b reveals the upconversion luminescent images of the hidden information of "UCNP" and the football, in which the "UCNP" and football emit luminescent colors under 980 nm laser illumination, while the remaining parts of the butterfly is nonluminescent. Notably, the luminescent images in Figure 5b are inhomogeneous, which is due in part to plasmonic tuning effect. As shown in Figure 2, different sizes of nanodisks will produce different luminescence colors with varying intensities. The nanodisk sizes within the letters "UCNP" or the football are varying, and hence their luminescent images are nonuniform. In addition, imperfect distribution of UCNPs within each resonator due to the self-assembly process also contributes to the grainy appearance in the images. This added randomness to the image could further increase the level of security of the prints. Overall, Figure 5 demonstrates that luminescent prints of letters "UCNP" and a football are successfully hidden into a nonluminescent plasmonic color print of butterfly. Therefore, we encode different luminescent images into a plasmonic color print and further enhance the anti-counterfeiting strength.

In summary, we realized a new optical security print, TRUE color printing, by incorporating upconversion nanocrystals within gap plasmon resonator structures. Under bright field illumination, the structures appear as colorful plasmonic prints. Due to gap plasmon modes in the metal-insulator-metal nanostructures, two orders of magnitude of luminescence enhancement were achieved. Plasmonic enhanced radiative decay or/and plasmonic enhanced excitation were responsible for the luminescence enhancement. Moreover, through tuning the plasmonic resonances and matching them with the energy level transitions of upconversion nanocrystals, a variety of luminescence colors was realized by selectively manipulated different emission bands of UCNPs. We successfully hid different luminescent images into a plasmonic color print, which increased the secrecy level of our TRUE color printing as optical security method.

Experimental Section

Materials: Yttrium(III) acetate hydrate ($Y(CH_3CO_2)_3$; 99.9%), gadolinium (III) acetate hydrate ($Gd(CH_3CO_2)_3$; 99.9%), ytterbium (III) acetate hydrate ($Yb(CH_3CO_2)_3$; 99.9%), erbium (III) acetate hydrate ($Er(CH_3CO_2)_3$; 99.9%), sodium hydroxide (NaOH; > 98%), ammonium fluoride (NH_4F; > 98%), oleic acid (OA) (90%), and 1-octadecene (ODE) (90%). All chemicals were used as received without further purification.

$NaGdF_4$:Yb,Er Preparation: 2.0 mL aqueous solution of $Gd(Ac)_3$ (0.4 mmol), $Yb(Ac)_3$ (0.09 mmol), $Er(Ac)_3$ (0.01 mmol), and OA (2.0 mL) was mixed and heated to 150 °C in an oil bath until a clear solution was formed, followed by the addition of ODE (7.5 mL) into the solution. The temperature was further maintained for 1.5 h and cooled naturally to room temperature. A solution of NaOH (1.25 mmol) and NH_4F (2.0 mmol) in methanol (5.0 mL) was added and the mixture was stirred overnight at room temperature. The reaction mixture was then heated at 100 °C, while being degassed for 30 min to remove methanol and residual moisture. Subsequently, the solution was heated to 285 °C and maintained for 1.5 h under a gentle argon flow. Finally, the solution was naturally cooled to room temperature. As-synthesized nanoparticles were collected by centrifugation and washed twice with ethanol. The nanoparticles were then dispersed in 5 mL of cyclohexane for further use.

$NaYF_4$:Yb,Er Preparation: 2.0 mL aqueous solution of $Y(Ac)_3$ (0.32 mmol), $Yb(Ac)_3$ (0.072 mmol), and $Er(Ac)_3$ (0.008 mmol) was added to a 50 mL flask containing 3 mL of oleic acid. The mixture was heated to 150 °C in an oil bath until a clear solution was formed, followed by the addition of 7 mL ODE into the solution. The temperature was further maintained for 1.5 h and cooled naturally to room temperature. A solution of NaOH (1.0 mmol) and NH_4F (1.6 mmol) in methanol (4 mL) was added and the mixture was stirred at 50 °C followed by heating to 100 °C. After the methanol was evaporated, the solution was heated to 290 °C and maintained for 2 h under a gentle argon flow. Finally, the solution was naturally cooled to room temperature. As-synthesized nanoparticles were collected by centrifugation and washed twice with ethanol. The nanoparticles were then dispersed in 4 mL of cyclohexane for further use.

Preparation of Hydrophilic Ligand Free UCNPs: The as-prepared oleic acid-capped nanoparticles were dispersed in the mixture containing 1 mL of ethanol and 1 mL of 0.2 M HCl solution. The resulting mixture

was sonicated for 5 min to remove the surface ligands, followed by centrifugation at 16 500 rpm for 20 min. The resulting products were washed with ethanol and H_2O several times and redispersed in H_2O.

Sample Fabrication: The samples were fabricated with the following steps. First, 100 nm Al film was deposited onto a silicon substrate with electron beam evaporator (Kurt J. Lesker) at deposition rate of 1.5 Å s^{-1}, and then a positive tone resist, PMMA (950K A4, Microchem) was spin-coated onto the Al film with rotation speed of 3500 rpm for 1 min. The sample was baked for 3 min at 150 °C. Second, different sizes of nanoholes were achieved with electron beam lithography (Raith, eLINE Plus) at 30 kV and the standard developing process. Third, 5 mg mL^{-1} NaGdF$_4$:Yb,Er or NaGdF$_4$ water solution was spin-coated onto the surface of the patterned PMMA, and followed by baking the sample for 5 min at 90 °C. Finally, 7.5 nm SiO$_2$ and 40 nm Al were sequentially deposited with electron beam evaporator (Kurt J. Lesker) to tightly seal the NaGdF$_4$:Yb,Er or NaGdF$_4$ in the gaps, and the plasmonic pixel arrays or color prints were achieved with the standard lift-off process in acetone.

SEM and TEM: The SEM images were scanned with eLINE Plus system (Raith) at acceleration voltage of 10 kV and aperture size of 30 μm. TEM images were obtained by a JEM-2100F transmission electron microscope at an acceleration voltage of 200 kV.

Optical Characterization: Reflectance spectra were measured with a micro-spectrophotometer (CRAIC) equipped with a 100 × lens (NA = 0.9). Reflectivity of a bulk Al mirror was measured as the reference signal. All the optical microscopy images of plasmonic color patches and prints were collected with the same microscope system.

Upconversion Luminescence: Upconversion luminescence microscopy images were collected on an Olympus BX51 microscope with the Xenon lamp adapted to a 980 nm CW laser. Upconversion luminescence spectra were measured with Ocean Optics QE Pro spectrometer connected to the microscope with 100 × lens (NA = 0.9). The spot size was set as 20 μm for spectral measurement, and the excitation power was 60 mW. The integration time for spectral measurement and image scanning was 400 ms.

Simulations: The simulated reflectance spectra and near-field electric field distributions were calculated with commercial software (FDTD, Lumerical Solutions). The wavelength-dependent refractive index of aluminum was taken from Palik, and the refractive indices of NaGdF$_4$:Yb,Er and SiO$_2$ were set as 1.4. Periodic boundary conditions were employed to accurately simulate the optical properties of pixel arrays, and the mesh sizes were set as $1 \times 1 \times 1$ nm^3. In the experiment an objective lens (100 ×, NA 0.9) was employed, thus part of the incident light was simulated with inclination angle to get the asymmetrical modes both in transverse electric (TE) and transverse magnetic (TM) cases. The Purcell factor, radiative decay rate and far-field radiation pattern were calculated by inserting a dipole into the ultrasmall gap. To simulate the incoherent, isotropic emission from UCNPs in the gap, dipoles along *x*, *y*, and *z* directions were placed in the same position in sequential simulations to get the averaged performance, furthermore, equally spaced positions in the gap to include the impact of position to the dipole emission were chosen. The results were obtained by integrating the data from different dipole directions and positions according to the rotational symmetry of the structure used.

Supporting Information

Supporting Information is available from the Wiley Online Library or from the author.

Acknowledgements

Conflict of Interest

The authors declare no conflict of interest.

Keywords

[1] F. Wang, X. Liu, *Chem. Soc. Rev.* **2009**, *38*, 976.

[2] J. Zhou, Q. Liu, W. Feng, Y. Sun, F. Li, *Chem. Rev.* **2015**, *115*, 395.

[3] J. H. Zeng, J. Su, Z. H. Li, R. X. Yan, Y. D. Li, *Adv. Mater.* **2005**, *17*, 2119.

[4] J. Butet, P.-F. Brevet, O. J. Martin, *ACS Nano* **2015**, *9*, 10545.

[5] K. Thyagarajan, J. Butet, O. J. Martin, *Nano Lett.* **2013**, *13*, 1847.

[6] P. Biagioni, M. Celebrano, M. Savoini, G. Grancini, D. Brida, S. Mátéfi-Tempfli, M. Mátéfi-Tempfli, L. Duò, B. Hecht, G. Cerullo, M. Finazzi, *Phys. Rev. B* **2009**, *80*, 045411.

[7] X. Zhu, Q. Su, W. Feng, F. Li, *Chem. Soc. Rev.* **2017**, *46*, 1025.

[8] S. Wu, G. Han, D. J. Milliron, S. Aloni, V. Altoe, D. V. Talapin, B. E. Cohen, P. J. Schuck, *Proc. Natl. Acad. Sci. USA* **2009**, *106*, 10917.

[9] L. Wang, R. Yan, Z. Huo, L. Wang, J. Zeng, J. Bao, X. Wang, Q. Peng, Y. Li, *Angew. Chem., Int. Ed.* **2005**, *44*, 6054.

[10] D. K. Chatterjee, M. K. Gnanasammandhan, Y. Zhang, *Small* **2010**, *6*, 2781.

[11] M. Lin, Y. Zhao, S. Wang, M. Liu, Z. Duan, Y. Chen, F. Li, F. Xu, T. Lu, *Biotechnol. Adv.* **2012**, *30*, 1551.

[12] R. Deng, F. Qin, R. Chen, W. Huang, M. Hong, X. Liu, *Nat. Nanotechnol.* **2015**, *10*, 237.

[13] T. R. Hinklin, S. C. Rand, R. M. Laine, *Adv. Mater.* **2008**, *20*, 1270.

[14] H. Ding, L. Lu, Z. Shi, D. Wang, L. Li, X. Li, Y. Ren, C. Liu, D. Cheng, H. Kim, N. C. Giebink, X. Wang, L. Yin, L. Zhao, M. Luo, X. Sheng, *Proc. Natl. Acad. Sci. USA* **2018**, *115*, 6632.

[15] A. Shalav, B. S. Richards, M. A. Green, *Sol. Energy Mater. Sol. Cells* **2007**, *91*, 829.

[16] S. Fischer, J. C. Goldschmidt, P. Löper, G. H. Bauer, R. Brüggemann, K. Krämer, D. Biner, M. Hermle, S. W. Glunz, *J. Appl. Phys.* **2010**, *108*, 044912.

[17] C.-J. Sun, Z. Xu, B. Hu, G. Yi, G. Chow, J. Shen, *Appl. Phys. Lett.* **2007**, *91*, 191113.

[18] Y. Lu, J. Zhao, R. Zhang, Y. Liu, D. Liu, E. M. Goldys, X. Yang, P. Xi, A. Sunna, J. Lu, Y. Shi, R. C. Leif, Y. Huo, J. Shen, J. A. Piper, J. P. Robinson, D. Jin, *Nat. Photonics* **2014**, *8*, 32.

[19] J. M. Meruga, W. M. Cross, P. S. May, Q. Luu, G. A. Crawford, J. J. Kellar, *Nanotechnology* **2012**, *23*, 395201.

[20] M. You, J. Zhong, Y. Hong, Z. Duan, M. Lin, F. Xu, *Nanoscale* **2015**, *7*, 4423.

[21] L. L. da Luz, R. Milani, J. F. Felix, I. R. Ribeiro, M. Talhavini, B. A. Neto, J. Chojnacki, M. O. Rodrigues, S. A. Junior, *ACS Appl. Mater. Interfaces* **2015**, *7*, 27115.

[22] M. You, M. Lin, S. Wang, X. Wang, G. Zhang, Y. Hong, Y. Dong, G. Jin, F. Xu, *Nanoscale* **2016**, *8*, 10096.

[23] S. Xie, C. Tong, H. Tan, N. Li, L. Gong, J. Xu, L. Xu, C. Zhang, *Mater. Chem. Front.* **2018**, *2*, 1997.

[24] T. Sun, B. Xu, B. Chen, X. Chen, M. Li, P. Shi, F. Wang, *Nanoscale* **2017**, *9*, 2701.

[25] M. Sy, A. Nonat, N. Hildebrandt, L. J. Charbonniere, *Chem. Commun.* **2016**, *52*, 5080.

[26] S. Han, X. Qin, Z. An, Y. Zhu, L. Liang, Y. Han, W. Huang, X. Liu, *Nat. Commun.* **2016**, *7*, 13059.

[27] G. Chen, H. Qiu, P. N. Prasad, X. Chen, *Chem. Rev.* **2014**, *114*, 5161.

[28] W. Niu, S. Wu, S. Zhang, L. Li, *Chem. Commun.* **2010**, *46*, 3908.

[29] S. Schietinger, L. d. S. Menezes, B. r. Lauritzen, O. Benson, *Nano Lett.* **2009**, *9*, 2477.

[30] Q. Shao, G. Zhang, L. Ouyang, Y. Hu, Y. Dong, J. Jiang, *Nanoscale* **2017**, *9*, 12132.

[31] Y. Han, H. Li, Y. Wang, Y. Pan, L. Huang, F. Song, W. Huang, *Sci. Rep.* **2017**, *7*, 1320.

[32] S. A. Maier, *Plasmonics: Fundamentals and Applications*, Springer, New York, USA **2007**.

[33] J. A. Schuller, E. S. Barnard, W. Cai, Y. C. Jun, J. S. White, M. L. Brongersma, *Nat. Mater.* **2010**, *9*, 193.

[34] H. Liu, Z. Wang, J. Huang, Y. J. Liu, H. J. Fan, N. I. Zheludev, C. Soci, *Nano Lett.* **2014**, *14*, 5162.

[35] K. Tanaka, E. Plum, J.-Y. Ou, T. Uchino, N. Zheludev, *Phys. Rev. Lett.* **2010**, *105*, 227403.

[36] S. Butun, S. Tongay, K. Aydin, *Nano Lett.* **2015**, *15*, 2700.

[37] F. Tam, G. P. Goodrich, B. R. Johnson, N. J. Halas, *Nano Lett.* **2007**, *7*, 496.

[38] H. Zhang, Y. Li, I. A. Ivanov, Y. Qu, Y. Huang, X. Duan, *Angew. Chem., Int. Ed.* **2010**, *49*, 2865.

[39] W. Zhang, F. Ding, S. Y. Chou, *Adv. Mater.* **2012**, *24*, OP236.

[40] H. P. Paudel, L. Zhong, K. Bayat, M. F. Baroughi, S. Smith, C. Lin, C. Jiang, M. T. Berry, P. S. May, *J. Phys. Chem. C* **2011**, *115*, 19028.

[41] M. Saboktakin, X. Ye, S. J. Oh, S.-H. Hong, A. T. Fafarman, U. K. Chettiar, N. Engheta, C. B. Murray, C. R. Kagan, *ACS Nano* **2012**, *6*, 8758.

[42] K. T. Lee, J. H. Park, S. J. Kwon, H. K. Kwon, J. Kyhm, K. W. Kwak, H. S. Jang, S. Y. Kim, J. S. Han, S. H. Lee, D. H. Shin, H. Ko, I. K. Han, B. K. Ju, S. H. Kwon, D. H. Ko, *Nano Lett.* **2015**, *15*, 2491.

[43] N. J. Greybush, M. Saboktakin, X. Ye, C. Della Giovampaola, S. J. Oh, N. E. Berry, N. Engheta, C. B. Murray, C. R. Kagan, *ACS Nano* **2014**, *8*, 9482.

[44] D. M. Wu, A. Garcia-Etxarri, A. Salleo, J. A. Dionne, *J. Phys. Chem. Lett.* **2014**, *5*, 4020.

[45] J. He, W. Zheng, F. Ligmajer, C. F. Chan, Z. Bao, K. L. Wong, X. Chen, J. Hao, J. Dai, S. F. Yu, D. Y. Lei, *Light: Sci. Appl.* **2017**, *6*, e16217.

[46] K. Park, K. Jung, S. J. Kwon, H. S. Jang, D. Byun, I. K. Han, H. Ko, *Adv. Funct. Mater.* **2016**, *26*, 7836.

[47] A. El Halawany, S. He, H. Hodaei, A. Bakry, M. A. Razvi, A. Alshahrie, N. J. Johnson, D. N. Christodoulides, A. Almutairi, M. Khajavikhan, *Opt. Express* **2016**, *24*, 13999.

[48] F. Kang, J. He, T. Sun, Z. Y. Bao, F. Wang, D. Y. Lei, *Adv. Funct. Mater.* **2017**, *27*, 1701842.

[49] S. J. Kwon, G. Y. Lee, K. Jung, H. S. Jang, J. S. Park, H. Ju, I. K. Han, H. Ko, *Adv. Mater.* **2016**, *28*, 7899.

[50] S. Schietinger, T. Aichele, H. Q. Wang, T. Nann, O. Benson, *Nano Lett.* **2010**, *10*, 134.

[51] A. Kristensen, J. K. W. Yang, S. I. Bozhevolnyi, S. Link, P. Nordlander, N. J. Halas, N. A. Mortensen, *Nat. Rev. Mater.* **2017**, *2*, 16088.

[52] K. Kumar, H. Duan, R. S. Hegde, S. C. Koh, J. N. Wei, J. K. Yang, *Nat. Nanotechnol.* **2012**, *7*, 557.

[53] X. Duan, S. Kamin, N. Liu, *Nat. Commun.* **2017**, *8*, 14606.

[54] Z. Dong, J. Ho, Y. F. Yu, Y. H. Fu, R. Paniagua-Dominguez, S. Wang, A. I. Kuznetsov, J. K. W. Yang, *Nano Lett.* **2017**, *17*, 7620.

[55] F. Ding, Y. Yang, R. A. Deshpande, S. I. Bozhevolnyi, *Nanophotonics* **2018**, *7*, 1129.

[56] M. Kuttge, F. J. Garcia de Abajo, A. Polman, *Nano Lett.* **2010**, *10*, 1537.

[57] G. M. Akselrod, C. Argyropoulos, T. B. Hoang, C. Ciracì, C. Fang, J. Huang, D. R. Smith, M. H. Mikkelsen, *Nat. Photonics* **2014**, *8*, 835.

[58] R. Carminati, J. J. Greffet, C. Henkel, J. M. Vigoureux, *Opt. Commun.* **2006**, *261*, 368.

[59] W. Park, D. Lu, S. Ahn, *Chem. Soc. Rev.* **2015**, *44*, 2940.